NANO LETTERS

pubs.acs.org/NanoLett

Letter

Nonvolatile Electro-optic Response of Graphene Driven by Ferroelectric Polarization

Jianghong Wu, Jialing Jian, Hui Ma, Yuting Ye, Bo Tang, Zhuang Qian, Qingyan Deng, Boshu Sun, Shi Liu, Hongtao Lin, and Lan Li*

Cite This: *Nano Lett.* 2024, 24, 11469−11475

Read Online

ACCESS | Metrics & More | Article Recommendations | Supporting Information

ABSTRACT: Two-dimensional materials (2DMs) have exhibited remarkably tunable optical characteristics, which have been applied for significant applications in communications, sensing, and computing. However, the reported tunable optical properties of 2DMs are almost volatile, impeding them in the applications of multifarious emerging frameworks such as programmable operation and neuromorphic computing. In this work, nonvolatile electro-optic response is developed by the graphene−Al_2O_3−In_2Se_3 heterostructure integrating with microring resonators (MRRs). In such compact devices, the optical absorption coefficient of graphene is substantially tuned by the out-of-plane ferroelectric polarization in α-In_2Se_3, resulting in a nonvolatile optical transmission in MRRs. This work demonstrates that integrating graphene with ferroelectric materials paves the way to develop nonvolatile devices in photonic circuits for emerging applications such as optical neural networks.

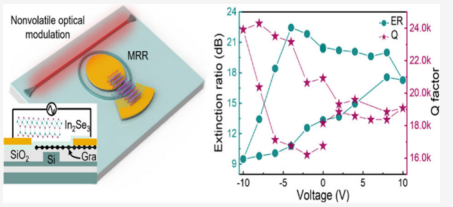

KEYWORDS: *In_2Se_3, graphene, ferroelectric polarization, nonvolatile electro-optic response, integrated photonics*

The increasing demands of precise optical modulation for optical communications, sensing, and computing, especially in integrated photonic circuits, have witnessed the requirement of new optical materials and novel device architectures.[1−6] In the past decade, two-dimensional materials (2DMs) with tunable optical characteristics induced by various stimulation and back-end CMOS-compatibility for different photonic platforms have been regarded as a competitive alternative for both optical intensity and phase modulation in integrated photonics.[7−12] For instance, graphene demonstrates both an absorptive and refractive index tunability for optical modulators via optical and electrical excitation with a small footprint and large extinction ratio.[13−16] However, the optical characteristics virtually turn back to the initial state accompanied with the external stimuli cancellation in these reported graphene devices, namely, volatile optical modulation.[17,18] These volatile devices require continuous power supply to maintain the functionality, limiting their potential use in large-scale programmable photonic integrated circuits for emerging applications such as optical neural networks, massive interference networks, and light detection and ranging.[19−21] Therefore, it is urgent and imperative to develop nonvolatile optical devices to overcome this bottleneck, thereby expediting and extending the applications in integrated photonics.

Recently, 2DMs with ferroelectricity have been a hotspot for exploring nonvolatile electrical memories by electrically triggering the ferroelectric domain.[22−26] These 2D ferroelectric materials exhibit a long retention time with ultrafast logic operation and high thermodynamic stability due to the absence of dangling bonds.[27−29] Intriguingly, the electrically controllable polarization switching in 2D ferroelectric materials has been applied to modify carrier concentration in graphene, thereby developing nonvolatile electrical memories.[30−32] For instance, nonvolatile electrical conductivity has been realized by electrically manipulating the out-of-plane electric dipoles of α-In_2Se_3 and $CuInP_2S_6$ in a graphene/Al_2O_3/In_2Se_3 hybrid field-effect transistor (FET) and a graphene/$CuInP_2S_6$ heterojunction.[33,34] In other words, the carrier concentration in graphene can be tuned by ferroelectric polarization, even in the absence of an external bias voltage, allowing for long-term stability. This behavior has significant implications for optical devices, as it enables the utilization of a tunable refractive index in graphene without a continuous voltage supply, catering to diverse applications that need rapid, energy-efficient, and dependable optical modulation. However, the application of this physical process has not been realized in the optical domain until now.

In this work, a nonvolatile electro-optic response has been observed in a microring resonator (MRR) integrating with a graphene/insulator/ferroelectric semiconductor (FeS-SMOS) structure. The ferroelectric semiconductor applied here is multilayer In_2Se_3, which possesses ferroelectricity even at the monolayer, maintains weak optical absorption at telecom

Received: June 4, 2024
Revised: August 27, 2024
Accepted: August 29, 2024
Published: September 3, 2024

https://doi.org/10.1021/acs.nanolett.4c02625
Nano Lett. 2024, 24, 11469−11475

bands due to an optical bandgap of 1.4 eV, and demonstrates the potential of the feasibility for large-scale growth.[35] Based on this hybrid waveguide, a nonvolatile optical tunability can be materialized by electrically regulating the polarity of the polarization-bound charge of In_2Se_3 that contributes to tuning the refractive index in graphene by altering carrier concentration, thereby bringing about a nonvolatile optical transmission change in an MRR. All in all, such an FeS-SMOS structure leads to the convenient integration with arbitrary integrated photonic platforms, including Si, SiN_x, and polymer, to demonstrate nonvolatile optical devices and thus promote the development of integrated photonic circuits in diverse emerging applications such as optical neural networks, optical neuromorphic computing, and quantum information processing.

A metal−ferroelectric oxide dielectric−semiconductor (Fe-MOS) structure is an available structure for nonvolatile electrical devices, where induced charges in a semiconductor can be electrically tuned by out-of-plane polarization inside the ferroelectric dielectric in Figure 1a, leading to a conductivity

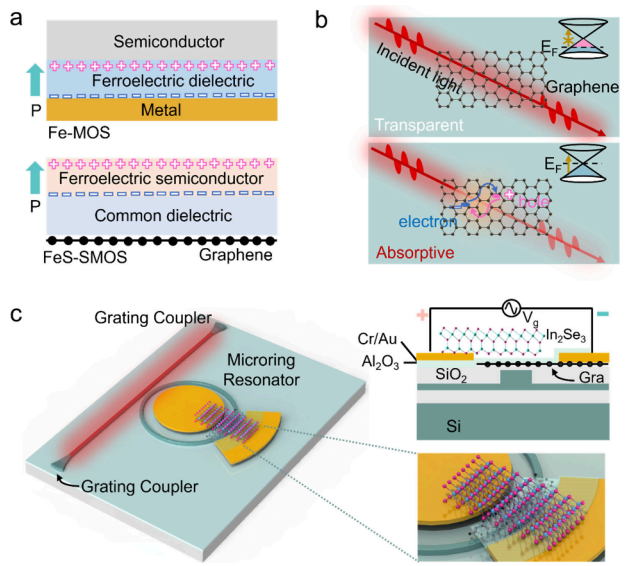

Figure 1. Device geometry and operational mechanism. (a) Schematics of the metal−ferroelectric oxide dielectric−semiconductor (Fe-MOS) structure and semimetal−oxide−ferroelectric semiconductor structure (FeS-SMOS). The polarization-bound charges are distributed inside the ferroelectric materials, and "P" represents the polarization direction. (b) Tunable interband absorption in graphene due to Pauli blocking, where it is almost transparent with electron depletion (illustrated by the Fermi level far away from the Dirac point), but it exhibits optical absorption at the intrinsic state when the Fermi level aligns with the Dirac point. (c) Schematic of a nonvolatile optical device based on a graphene/Al_2O_3/In_2Se_3 FeS-SMOS structure on an MRR. The chart in the bottom right corner is the magnified view of the overlapping region between FeS-SMOS and MRR. The cross-section in the upper right corner diagram shows that the Al_2O_3 layer is inserted between graphene and In_2Se_3 to construct a parallel-plate capacitor.

change. This structure integrating with an optical waveguide, however, brings about substantial optical loss induced by metal absorption at telecom bands, deteriorating the optical tunability ability. In this work, we replace the metal film with graphene on the MRRs to minimize optical loss in a hybrid optical waveguide. Simultaneously, a ferroelectric semiconductor substitutes for the ferroelectric dielectric to provide a stable polarization (bottom schematic in Figure 1a), which also offers the advantage of alleviating fabrication limitations since the majority of high-quality amorphous insulators can be used in the FeS-SMOS structure. In this FeS-SMOS architecture, the induced charge concentration in monolayer graphene can be tuned by the out-of-plane ferroelectric polarization field in the In_2Se_3 flake with retentive properties for nonvolatile operation. Meanwhile, due to Pauli blocking effect, the tunable carrier concentration results in a remarkable change of refractive index, especially for the interband absorption coefficient.[36] Specifically, graphene brings about a negligible optical absorption at the telecom C band when the energy difference between the Dirac point and the Fermi level is larger than 0.4 eV (upper schematic in Figure 1b). On the contrary, an apparent optical loss can be induced by intrinsic and slightly doped graphene as a consequence of semimetal characteristics, with the generation of photoinduced electron−hole pairs (bottom schematic in Figure 1b).[37]

Considering both the doping effect by the ferroelectric polarization and tunable optical absorption in graphene integration, a nonvolatile optical device is proposed by integrating the FeS-SMOS structure with an MRR, in which two grating couplers feed light in and out of the optical waveguide and MRR (Figure 1c). In this device, an optical ridge waveguide with 150 nm height and 500 nm width can support the fundamental mode of transverse electric polarization (TE_0) at the telecom C band in Figure S1 (Supporting Information). Monolayer graphene is located on an optical waveguide, with an Al_2O_3 dielectric inserted between graphene and In_2Se_3, consisting of a vertical parallel-plate capacitor (upper-right schematic in Figure 1c). In this device, optical absorption tunability in graphene can be carried out by regulating the direction and proportion of the ferroelectric domain within In_2Se_3, thereby effectively altering the coupling state within an MRR and achieving a nonvolatile electro-optic response.

In_2Se_3 is a polymorphic material and exhibits numerous crystalline phases such as α, β', β, and γ phases.[38,39] Among these different phases, α-In_2Se_3 demonstrates inherent out-of-plane ferroelectricity with reversible spontaneous polarization verified in both theoretical calculation and experimental observation.[40] The Raman spectrum of multilayer In_2Se_3 (~50 nm thick) excited at the wavelength of 532 nm displays four characteristic peaks at 89, 104, 187, and 194 cm^{-1} (Figure S5d (Supporting Information)), resulting from the phonon vibration of E^2, A_1 (LO + TO), A_1 (LO), and A_1 (TO) modes, indicating that the In_2Se_3 flake used in our experiment is hexagonal α phase. Simultaneously, the X-ray diffraction pattern in Figure S3 (Supporting Information) shows c-plane peaks and high-order interplanar spacing, belonging to hexagonal α-In_2Se_3.[41] Furthermore, the exploited In_2Se_3 flake exhibits strong second-harmonic generation in Figures S3b,c (Supporting Information), which can be attributed to the broken inversion symmetry of α-In_2Se_3. Additionally, an apparent photoluminescence (PL) signal can also be observed in Figure S3d (Supporting Information), showing a peak at the wavelength of 863 nm, which corresponds to an optical bandgap of approximately 1.44 eV. This optical bandgap is larger than the photon energy at the telecom band, thereby introducing a slight insertion loss in the hybrid optical waveguide. Attentively, all In_2Se_3 flakes in this work are in the hexagonal α phase.

https://doi.org/10.1021/acs.nanolett.4c02625
Nano Lett. 2024, 24, 11469−11475

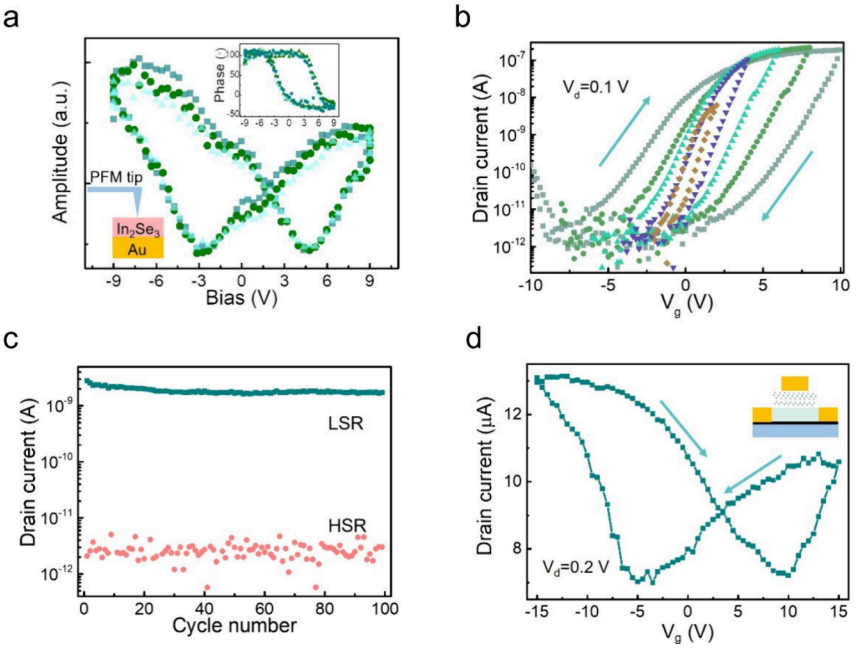

Figure 2. Characterizations of ferroelectric properties. (a) Off-field piezoelectric force microscopy (PFM) amplitude and phase (illustration in the upper-right corner); hysteresis loops of the In_2Se_3 flake (60 nm thick) on the Au substrate supported by the SiO_2/Si substrate (illustration in the bottom-left corner). (b) Transfer curves of a typical In_2Se_3 FET (V_d = 0.1 V). (c) Endurance characterization of the In_2Se_3 FET, with write, erase, and read (V_d) voltages of ±10 and 0.1 V, respectively; two states are named low-resistance state (LRS) and high-resistance state (HRS). (d) Transfer curve of a graphene/Al_2O_3/In_2Se_3 FET (V_d = 0.2 V). The blue, black, green, and yellow cubes in the illustration are the substrate, graphene, Al_2O_3, and Cr/Au pad. In_2Se_3 is inserted between Al_2O_3 and the top gate electrode.

Subsequently, we characterized the ferroelectric properties of multilayer In_2Se_3 flakes. First, mechanically exfoliated In_2Se_3 was transferred onto a Au film (illustration in Figure 2a) to conduct characterization by piezoresponse force microscopy (PFM). A sensible piezoelectric response can be observed for a 60 nm-thick In_2Se_3 flake according to the measured PFM amplitude and phase versus voltage hysteresis loops (Figure 2a), demonstrating obvious ferroelectric polarization switching driven by an external electric field, which is consistent with the results in previous reports.[27] After that, the In_2Se_3 FET was prepared with a 15 nm-thick Al_2O_3 dielectric serving as a gate insulator (bottom-gate configuration), and the detailed information for the In_2Se_3 FET is shown in Figure S4 (Supporting Information). Transfer curves (I_d−V_g) of a typical In_2Se_3 FET (Figure 2b) under different sweeping gate voltage (V_g) at a fixed source−drain voltage (V_d = 0.1 V) imply a high on/off ratio over 10^5. Concurrently, the clockwise hysteresis loop remains, and the memory window enlarges with the incremental gate voltage, signifying that the degree of ferroelectric polarization can be electrically tuned by different V_g. After that, the endurance performance of nonvolatile electrical memory was checked at the write/erase and read voltages of ±10 and 0.1 V, and two stable states of LRS and HRS can be observed (Figure 2c) as a result of polarity switching of the polarization bound charge. These robust measurements confirm the presence of out-of-plane ferroelectricity in In_2Se_3, revealing the potential for nonvolatile optical devices. Moreover, polarization stability in In_2Se_3 has been validated in the previous report, showing a stable ferroelectric polarization with a long retention time for practical applications.[42] Additionally, the transfer curve (Figure 2d) of a graphene/Al_2O_3/In_2Se_3 shows a nonvolatile butterfly-like dependence on gate voltage, indicating that the Fermi level in graphene can be tuned by ferroelectric polarization in In_2Se_3.

We then designed a series of MRRs (diameter: 80 μm) with different gaps between the straight waveguide and rings ranging from 200 to 400 nm (with an interval of 50 nm) in Figure 3a, whose transmission spectra have been characterized in our previous report.[43] Generally, chemical vapor deposition-grown graphene is slightly p-doped and works as an optical loss medium at the telecom band; thereby overcoupled and critically coupling MRRs in the initial state are more suitable for demonstrating graphene-integrated electro-optic modulators. The obtained waveguide-integrated devices show a clean appearance (Figure 3a), benefiting from minimal contamination during both wet and dry transfer processes. Limited fractures and wrinkles upon graphene were introduced during the wet transfer process, proven by optical microscope images in Figure S5a,b (Supporting Information). Simultaneously, the absence of defect peaks in Raman indicates that atom defects would not be generated during Al_2O_3 deposition by atomic layer deposition (ALD) in Figure S5c (Supporting Information), while there is slight interference of the doping level proven by the reduction of the intensity ratio (I_{2D}/I_G).[44] The high-magnification device configuration was conducted by SEM in Figure 3b, showing an FeS-SMOS structure on the arm of an MRR, and the In_2Se_3 thickness is about 44 nm in this device in Figure S6a (Supporting Information). As expected, a low loss of mode-mismatching can be observed in a Si/SiO_2/graphene/Al_2O_3/In_2Se_3 hybrid waveguide in Figure S1 (Supporting Information). Moreover, in-plane (E_x and E_z) and out-of-plane (E_y) electric field components of TE_0 modes are depicted in Figure S1b,c,d (Supporting Information), and obvious overlap between in-plane electric field components and graphene ensures effective light−matter interaction.

https://doi.org/10.1021/acs.nanolett.4c02625
Nano Lett. 2024, 24, 11469−11475

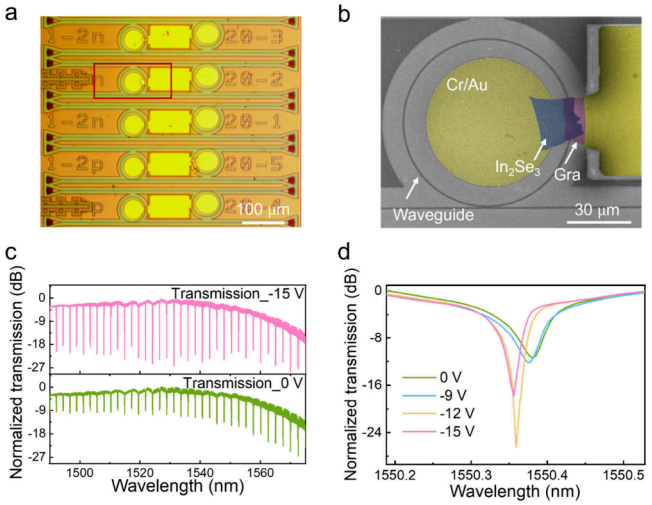

Figure 3. Tunable optical transmission. (a) Optical microscope image of the MRR array. A typical MRR-integrated graphene device is marked in the red rectangle. (b) A false-color high-magnification result characterized by scanning electron image (SEM). Blue, purple, and yellow regions represent In_2Se_3, graphene, and metal pads, respectively. A slight color difference between the two metal pads is induced by Al_2O_3 covering the right metal pad. (c) Optical transmission variation over a broad wavelength from 1490 to 1575 nm at V_g = 0 V and −15 V, respectively. (d) Tunable transmission around 1550 nm, with the applied V_g varying from 0 to −15 V. Al_2O_3 thickness in this device is 22 nm.

Transmission spectra were then recorded over broad wavelengths ranging from 1490 to 1575 nm. This MRR coupling with a hybrid waveguide is undercoupled because a larger ER is observed at the longer wavelength at the initial state (Figure 3c). At V_g = −15 V, an ER dramatically increases at those resonance wavelengths, and the largest ER becomes blue-shift as well, indicating that optical modulation can be operated across a wide wavelength range (Figure 3c) because of the semimetal property of graphene. Actually, grating couplers predominantly limit the optical bandwidth in this work, and a larger optical bandwidth can be realized by replacing the grating couplers with edge couplers. We then characterized optical transmission under different gate voltages (Figure 3d), where Al_2O_3 thickness is 22 nm in this device. Theoretically, graphene obtains a higher hole concentration with the larger absolute value of negative gate voltage (smaller than the breakdown voltage), and thus, small optical absorption is realized in this condition. Therefore, an MRR operates from an undercoupled (0 V) to a critically coupled condition (−12 V) and then to an overcoupled condition (−15 V), with ER first increasing and then decreasing, implying that the proposed FeS-SMOS structure is capable of obtaining a tunable optical response. Simultaneously, the slight resonance wavelength shift is primarily attributed to a non-monotonic electron-refractive response[45] and an electron-refractive response induced by polarization variation in In_2Se_3. A similar electron-refractive response in ferroelectric dielectrics has been observed.[46] Additionally, electrostatic doping heavily depends on the capacitance value, which can be expressed as $C = \varepsilon \times S/d$, where ε, S, and d are the dielectric constant, size, and distance of a parallel-plate capacitor, respectively. Therefore, the thickness of the Al_2O_3 dielectric is reduced to optimize the tunable efficiency via an electrostatic field, and a smaller V_g for optical modulation can be obtained when the Al_2O_3 dielectric is 15 nm thick, as shown in Figure S6a (Supporting Information).

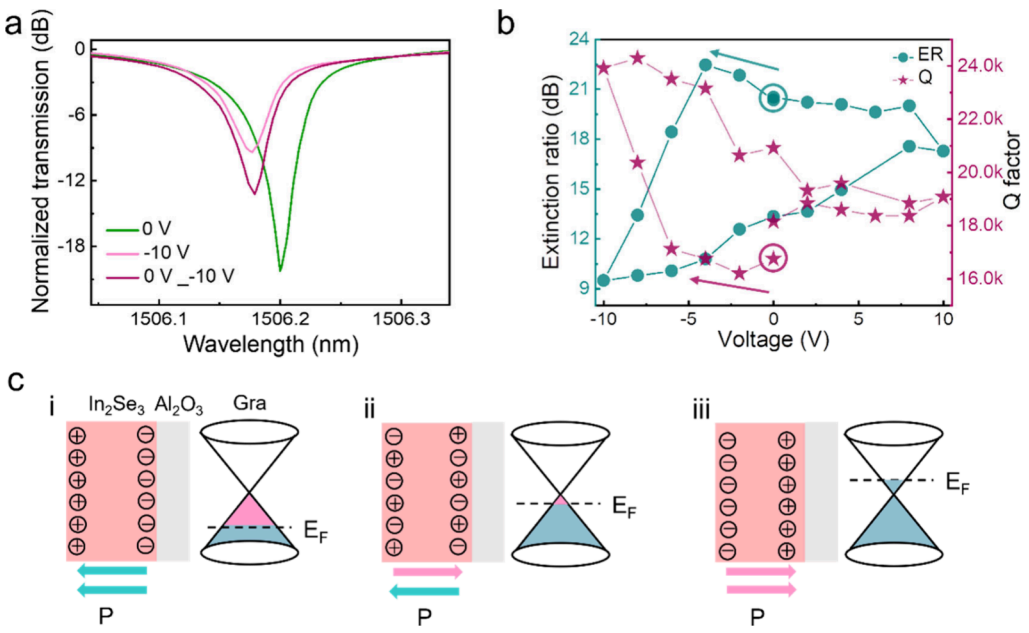

Figure 4. Nonvolatile functionality and mechanism. (a) Nonvolatile optical transmission based on the FeS-SMOS structure integrating with an MRR. The thickness of the Al_2O_3 dielectric is 15 nm in this device. (b) ER and quality (Q) factor variations at ∼1506 nm under different bias voltages. The two marked points by green and claret rings correspond to the ER and Q factor at the initial state. The green and red arrows represent the direction of the V_g change. V_g shifts from 0 to −10 V, and from −10 to 10 V, and then from 10 to 0 V, respectively. V_g's duration and measurement interval are 27 and 120 s, respectively. (c) Schematics for the working mechanism of nonvolatile adjustability of the Fermi level in graphene. (ii) Ferroelectric field has little impact on graphene in the initial condition, (i), and electron depletion occurs with the direction of polarization pointing to the left region. (iii) In contrast, electron accumulation occurs in the opposite direction of ferroelectric polarization.

https://doi.org/10.1021/acs.nanolett.4c02625
Nano Lett. 2024, 24, 11469−11475

The nonvolatile optical property was then experimentally checked. A typical MRR with an ER of 20.3 dB at ∼1506 nm in the initial state is adopted (Figure 4a), and the In_2Se_3 thickness is 45 nm in this device in Figure S6b (Supporting Information). At V_g = −10 V for a graphene/Al_2O_3/In_2Se_3 FeS-SMOS device, induced carriers excited by a synergistic effect of the electrostatic field and ferroelectric polarization result in electron depletion in monolayer graphene, thus bringing about smaller optical absorption. Under the circumstance, the diminished optical loss in the cavity makes an MRR vary from the critically coupled condition to the overcoupled condition, accompanied by ER decreasing from 20.3 dB to 9.5 dB (Figure 4a). Quite significantly, ER rises from 9.5 dB to 13.3 dB when the gate voltage changes from −10 to 0 V (Figure 4a), which is different from that in the initial condition, demonstrating the nonvolatile optical transmission. The difference in optical transmission between the initial condition (marked "0 V" in Figure 4a) and that under polarization pointing to graphene (marked "0 V_−10 V" in Figure 4a) is primarily attributed to the different electron concentration on graphene induced by the out-of-plane ferroelectric polarization. Additionally, optical transmission spectra under different conditions are collected to illustrate nonvolatile functionality in Figures S7b and c (Supporting Information), in which the optical transmission in an MRR is determined by both the current and the former applied gate voltage.

Significant parameters, including ERs and Q factors, were also measured to concretely reveal the nonvolatile characteristics. During the characterization of optical transmission, V_g changes from 0 V to −10 V, then increases from −10 V to 10 V, and finally returns from 10 V to 0 V. Intriguingly, the variable tendency of ER and Q on the gate voltage axis (Figure 4b) indicates the nonvolatile optical property, similar to that of current hysteresis loops (Figure 2c), which is principally attributed to tunable optical loss in an MRR driven by the out-of-plane ferroelectric polarization in In_2Se_3. Specifically, polarization-bound charges reassemble chaotically at the initial conditions (ii in Figure 4c). Thus, the electrostatic field in this FeS-SMOS structure primarily contributes to the carrier concentration variation in graphene as V_g shifts from 0 to −10 V, simultaneously leading to Q increasing from 1.7×10^4 to 2.4×10^4. On the contrary, robust ferroelectric polarization within In_2Se_3 is generated via the excitation of an external electrostatic field (V_g = −10 V), thereby carrier concentration in graphene controlled by the conjoint interaction of an electrostatic field and ferroelectric polarization with V_g varying from −10 to 0 V (i in Figure 4c). The above-mentioned description is consistent with the changes in ER and Q in Figure 4b. For instance, the contribution of electrostatic doping at −4 V (for that V_g starting from 0 V and from −10 V) is almost the same, but the D value ER and Q in these two states is 11.7 dB and 6.4×10^3 as a consequence of different ferroelectric polarization. Furthermore, ferroelectric polarization switching can be obtained by a reverse applied voltage larger than the threshold voltage to shift the polarity of the polarization bound charge, thus leading to electron accumulation in graphene (iii in Figure 4c). Therefore, optical loss gradually increases with electron injection in graphene under a positive gate voltage, accompanied by the reduced Q and increased ER, when V_g rises from 0 to 10 V. The asymmetric characteristics of ER and Q (Figure 4b) can be mainly attributed to the asymmetric graphene optical absorption change about the gate voltage at the telecom band as a result of the p-doped property.[7] In other words, smaller optical absorption can be realized for p-type graphene than that of n-type counterparts with the same doping concentration. Additionally, a slight nonvolatile shift of resonance wavelength (Figure S8) can be observed, which is probably attributed to refractive index variation induced by different ferroelectric polarization in In_2Se_3[47,48] and refractive response in graphene by ferroelectric doping.[49]

In summary, we observed the nonvolatile electro-optic response by integrating MRRs with a graphene/Al_2O_3/In_2Se_3 FeS-SMOS structure, which benefits from both the out-of-plane ferroelectric polarization in In_2Se_3 and tunable optical absorption in graphene because of Pauli blocking. In such hybrid devices, polarization switching of inner In_2Se_3 can be triggered by an external electrical field, and then the robust polarization can tune carrier concentration upon graphene, thus bringing about a measurable variation in optical absorption and a nonvolatile electro-optic response. The obtained nonvolatile functionality can significantly expedite and expand large-scale integrated photonic circuits for emerging applications, such as optical neural networks with low power consumption. Further development of nonvolatile ferroelectric optical devices probably involves minimizing the resistance-capacitance value in the FeS-SMOS structure and exploring alternative architectures, such as ferroelectric tunneling junctions, for superior efficiency.

■ ASSOCIATED CONTENT

Supporting Information

The Supporting Information is available free of charge at https://pubs.acs.org/doi/10.1021/acs.nanolett.4c02625.

Optical simulation, device fabrication processes, In_2Se_3 material characterization, optical image of In_2Se_3 FET and large-scale graphene, In_2Se_3 thickness characterization, transmission spectra characterization, resonance wavelength shift (PDF)

■ AUTHOR INFORMATION

Corresponding Author

Lan Li − *Key Laboratory of 3D Micro/Nano Fabrication and Characterization of Zhejiang Province, School of Engineering, Westlake University, Hangzhou 310024, China; Westlake Institute for Optoelectronics, Fuyang, Hangzhou 311421, China; Institute of Advanced Technology, Westlake Institute for Advanced Study, Hangzhou 310024, China;* orcid.org/0000-0002-9097-9157; Email: lilan@westlake.edu.cn

Authors

Jianghong Wu − *Key Laboratory of 3D Micro/Nano Fabrication and Characterization of Zhejiang Province, School of Engineering, Westlake University, Hangzhou 310024, China; Institute of Advanced Technology, Westlake Institute for Advanced Study, Hangzhou 310024, China; Department of Applied Physics, The Hongkong Polytechnic University, Hong Kong 999077, China*

Jialing Jian − *Key Laboratory of 3D Micro/Nano Fabrication and Characterization of Zhejiang Province, School of Engineering, Westlake University, Hangzhou 310024, China; Institute of Advanced Technology, Westlake Institute for Advanced Study, Hangzhou 310024, China;* orcid.org/0000-0001-6809-6588

https://doi.org/10.1021/acs.nanolett.4c02625
Nano Lett. 2024, 24, 11469−11475

Hui Ma − *State Key Laboratory of Modern Optical Instrumentation, College of Information Science and Electronic Engineering, Zhejiang University, Hangzhou 310027, China;* orcid.org/0000-0002-3670-0442
Yuting Ye − *Key Laboratory of 3D Micro/Nano Fabrication and Characterization of Zhejiang Province, School of Engineering, Westlake University, Hangzhou 310024, China; Institute of Advanced Technology, Westlake Institute for Advanced Study, Hangzhou 310024, China*
Bo Tang − *Institute of Microelectronics, Chinese Academic Society, Beijing 100029, China*
Zhuang Qian − *Key Laboratory for Quantum Materials of Zhejiang Province, Department of Physics, School of Science, Westlake University, Hangzhou 310024, China; Institute of Natural Sciences, Westlake Institute for Advanced Study, Hangzhou 310024, China*
Qingyan Deng − *Key Laboratory of 3D Micro/Nano Fabrication and Characterization of Zhejiang Province, School of Engineering, Westlake University, Hangzhou 310024, China; Institute of Advanced Technology, Westlake Institute for Advanced Study, Hangzhou 310024, China*
Boshu Sun − *Key Laboratory of 3D Micro/Nano Fabrication and Characterization of Zhejiang Province, School of Engineering, Westlake University, Hangzhou 310024, China; Institute of Advanced Technology, Westlake Institute for Advanced Study, Hangzhou 310024, China*
Shi Liu − *Key Laboratory for Quantum Materials of Zhejiang Province, Department of Physics, School of Science, Westlake University, Hangzhou 310024, China; Institute of Natural Sciences, Westlake Institute for Advanced Study, Hangzhou 310024, China;* orcid.org/0000-0002-8488-4848
Hongtao Lin − *State Key Laboratory of Modern Optical Instrumentation, College of Information Science and Electronic Engineering, Zhejiang University, Hangzhou 310027, China;* orcid.org/0000-0001-7432-3644

Complete contact information is available at: https://pubs.acs.org/10.1021/acs.nanolett.4c02625

Notes

The authors declare no competing financial interest.

■ ACKNOWLEDGMENTS

The authors thank the Westlake Center for Micro/Nano Fabrication and Instrumentation and ZJU Micro-Nano Fabrication Center at Zhejiang University for the facility support. The author thanks (Dr. Chen Zhong) Instrumentation and Service Center for Molecular Sciences at Westlake University for Raman, PL, and SHG measurement. The authors thank Zhengyang Chen for a discussion about ferroelectric characterization. The research was partially supported by the National Natural Science Foundation of China (Grant Numbers 12104375, 62175202, 61975179, 91950204), Key Project of Westlake Institute for Optoelectronics (2023GD003/110500Y0022303), Zhejiang Provincial Natural Science Foundation of China (LD22F040002), Leading Innovative and Entrepreneur Team Introduction Program of Zhejiang (2020R01005), and Special Support Plan for Photoelectric Chips Research at Westlake University (10300000H062201/004).

■ REFERENCES

(1) Shen, Y.; Harris, N. C.; Skirlo, S.; Prabhu, M.; Baehr-Jones, T.; Hochberg, M.; Sun, X.; Zhao, S.; Larochelle, H.; Englund, D.; Soljačić, M. Deep learning with coherent nanophotonic circuits. *Nat. Photonics* **2017**, *11*, 441−446.
(2) Tang, R.; Sun, C.; Bao, K.; Chen, Z.; Ju, Z.; Wei, M.; Wu, Y.; Wu, J.; Xu, K.; Lin, H.; Li, L. High-Resolution 2D Quasi-Distributed Optical Sensing with On-Chip Multiplexed FSR-Free Nanobeam Cavity Array. *Laser Photonics Rev.* **2024**, *18*, 2300828.
(3) Romagnoli, M.; Sorianello, V.; Midrio, M.; Koppens, F. H. L.; Huyghebaert, C.; Neumaier, D.; Galli, P.; Templ, W.; D'Errico, A.; Ferrari, A. C. Graphene-based integrated photonics for next-generation datacom and telecom. *Nat. Rev. Mater.* **2018**, *3*, 392−414.
(4) He, T.; Ma, H.; Wang, Z.; Li, Q.; Liu, S.; Duan, S.; Xu, T.; Wang, J.; Wu, H.; Zhong, F.; et al. On-chip optoelectronic logic gates operating in the telecom band. *Nat. Photonics* **2024**, *18*, 60−67.
(5) Dong, C.; An, X.; Wu, Z.; Zhu, Z.; Xie, C.; Huang, J.-A.; Luo, L. Multilayered $PdTe_2$/thin Si heterostructures as self-powered flexible photodetectors with heart rate monitoring ability. *J. Semicond.* **2023**, *44*, 112001.
(6) Sun, C.; Yin, Y.; Chen, Z.; Ye, Y.; Luo, Y.; Ma, H.; Wang, L.; Wei, M.; Jian, J.; Tang, R.; et al. Tunable narrow-band single-channel add-drop integrated optical filter with ultrawide FSR. *PhotoniX* **2022**, *3*, 12.
(7) Liu, M.; Yin, X.; Ulin-Avila, E.; Geng, B.; Zentgraf, T.; Ju, L.; Wang, F.; Zhang, X. A graphene-based broadband optical modulator. *Nature* **2011**, *474*, 64−67.
(8) Datta, I.; Chae, S. H.; Bhatt, G. R.; Tadayon, M. A.; Li, B.; Yu, Y.; Park, C.; Park, J.; Cao, L.; Basov, D.; et al. Low-loss composite photonic platform based on 2D semiconductor monolayers. *Nat. Photonics* **2020**, *14*, 256−262.
(9) Li, H.; Anugrah, Y.; Koester, S. J.; Li, M. Optical absorption in graphene integrated on silicon waveguides. *Appl. Phys. Lett.* **2012**, *101*, 111110.
(10) Sun, Z.; Martinez, A.; Wang, F. Optical modulators with 2D layered materials. *Nat. Photonics* **2016**, *10*, 227−238.
(11) Zhang, Y.; Wu, J.; Yang, Y.; Qu, Y.; El Dirani, H.; Crochemore, R.; Sciancalepore, C.; Demongodin, P.; Grillet, C.; Monat, C.; et al. Enhanced self-phase modulation in silicon nitride waveguides integrated with 2D graphene oxide films. *IEEE J. Sel. Top. Quantum Electron.* **2022**, *29*, 1−13.
(12) Zhang, Y.; Wu, J.; Qu, Y.; Jia, L.; Jia, B.; Moss, D. J. Optimizing the Kerr nonlinear optical performance of silicon waveguides integrated with 2D graphene oxide films. *J. Lightwave Technol.* **2021**, *39*, 4671−4683.
(13) Yu, S.; Wu, X.; Chen, K.; Chen, B.; Guo, X.; Dai, D.; Tong, L.; Liu, W.; Ron Shen, Y. All-optical graphene modulator based on optical Kerr phase shift. *Optica* **2016**, *3*, 541−544.
(14) Chen, K.; Zhou, X.; Cheng, X.; Qiao, R. X.; Cheng, Y.; Liu, C.; Xie, Y. D.; Yu, W. T.; Yao, F. R.; Sun, Z. P.; Wang, F.; Liu, K. H.; Liu, Z. F. Graphene photonic crystal fibre with strong and tunable light-matter interaction. *Nat. Photonics* **2019**, *13*, 754−759.
(15) Li, W.; Chen, B.; Meng, C.; Fang, W.; Xiao, Y.; Li, X.; Hu, Z.; Xu, Y.; Tong, L.; Wang, H.; Liu, W.; Bao, J.; Shen, Y. R. Ultrafast All-Optical Graphene Modulator. *Nano Lett.* **2014**, *14*, 955−959.
(16) Datta, I.; Gil-Molina, A.; Chae, S. H.; Zhou, V.; Hone, J.; Lipson, M. 2D material platform for overcoming the amplitude-phase tradeoff in ring resonators. *Optica* **2024**, *11*, 48−57.
(17) Ding, Y.; Zhu, X.; Xiao, S.; Hu, H.; Frandsen, L. H.; Mortensen, N. A.; Yvind, K. Effective electro-optical modulation with high extinction ratio by a graphene-silicon microring resonator. *Nano Lett.* **2015**, *15*, 4393−4400.
(18) Koester, S. J.; Li, M. Waveguide-coupled graphene optoelectronics. *IEEE J. Sel. Top. Quantum Electron.* **2014**, *20*, 84−94.
(19) Bogaerts, W.; Pérez, D.; Capmany, J.; Miller, D. A.; Poon, J.; Englund, D.; Morichetti, F.; Melloni, A. Programmable photonic circuits. *Nature* **2020**, *586*, 207−216.

(20) Peserico, N.; Shastri, B. J.; Sorger, V. J. Integrated Photonic Tensor Processing Unit for a Matrix Multiply: A Review. *J. Lightwave Technol.* **2023**, *41*, 3704−3716.
(21) Solyanik-Gorgone, M.; Kang, H.; Nouri, B. M.; Dalir, H.; Sorger, V. J. Hashing for secure optical information compression in a heterogeneous convolutional neural network. *Appl. Phys. Rev.* **2023**, *10*, 021412.
(22) Garcia-Ruiz, A.; Enaldiev, V.; McEllistrim, A.; Fal'ko, V. I. Mixed-Stacking Few-Layer Graphene as an Elemental Weak Ferroelectric Material. *Nano Lett.* **2023**, *23*, 4120−4125.
(23) Bian, R.; Cao, G.; Pan, E.; Liu, Q.; Li, Z.; Liang, L.; Wu, Q.; Ang, L. K.; Li, W.; Zhao, X.; Liu, F. High-Performance Sliding Ferroelectric Transistor Based on Schottky Barrier Tuning. *Nano Lett.* **2023**, *23*, 4595−4601.
(24) Li, X.; Chen, X.; Deng, W.; Li, S.; An, B.; Chu, F.; Wu, Y.; Liu, F.; Zhang, Y. An all-two-dimensional Fe-FET retinomorphic sensor based on the novel gate dielectric $In_2Se_{3-x}O_x$. *Nanoscale* **2023**, *15*, 10705−10714.
(25) Xue, F.; He, X.; Retamal, J. R. D.; Han, A.; Zhang, J.; Liu, Z.; Huang, J.-K.; Hu, W.; Tung, V.; He, J.-H.; Li, L.-J.; Zhang, X. Gate-Tunable and Multidirection-Switchable Memristive Phenomena in a Van Der Waals Ferroelectric. *Adv. Mater.* **2019**, *31*, 1901300.
(26) Xue, F.; Hu, W.; Lee, K.-C.; Lu, L.-S.; Zhang, J.; Tang, H.-L.; Han, A.; Hsu, W.-T.; Tu, S.; Chang, W.-H.; Lien, C.-H.; He, J.-H.; Zhang, Z.; Li, L.-J.; Zhang, X. Room-Temperature Ferroelectricity in Hexagonally Layered α-In_2Se_3 Nanoflakes down to the Monolayer Limit. *Adv. Funct. Mater.* **2018**, *28*, 1803738.
(27) Si, M.; Saha, A. K.; Gao, S.; Qiu, G.; Qin, J.; Duan, Y.; Jian, J.; Niu, C.; Wang, H.; Wu, W.; et al. A ferroelectric semiconductor field-effect transistor. *Nat. Electron.* **2019**, *2*, 580−586.
(28) He, Q.; Tang, Z.; Dai, M.; Shan, H.; Yang, H.; Zhang, Y.; Luo, X. Epitaxial Growth of Large Area Two-Dimensional Ferroelectric α-In_2Se_3. *Nano Lett.* **2023**, *23*, 3098−3105.
(29) Yang, J. Y.; Park, M.; Yeom, M. J.; Baek, Y.; Yoon, S. C.; Jeong, Y. J.; Oh, S. Y.; Lee, K.; Yoo, G. Reconfigurable Physical Reservoir in GaN/α-In_2Se_3 HEMTs Enabled by Out-of-Plane Local Polarization of Ferroelectric 2D Layer. *ACS Nano* **2023**, *17*, 7695−7704.
(30) Zhang, Y.; Taniguchi, R.; Masubuchi, S.; Moriya, R.; Watanabe, K.; Taniguchi, T.; Sasagawa, T.; Machida, T. Switchable out-of-plane shift current in ferroelectric two-dimensional material $CuInP_2S_6$. *Appl. Phys. Lett.* **2022**, *120*, 013103.
(31) Zhao, Z.; Xu, K.; Ryu, H.; Zhu, W. Strong Temperature Effect on the Ferroelectric Properties of $CuInP_2S_6$ and Its Heterostructures. *ACS Appl. Mater. Interfaces* **2020**, *12*, 51820−51826.
(32) Cheng, J. T.; Liu, K.; Zhao, X. J.; Xue, X. L.; Zhang, L. L.; Pang, R.; Ren, X. Y.; Li, S. F. Negative-positive oscillation in interfacial friction of a In_2Se_3-graphene heterojunction. *Phys. Rev. B* **2022**, *106*, 195416.
(33) Wan, S.; Li, Y.; Li, W.; Mao, X.; Wang, C.; Chen, C.; Dong, J.; Nie, A.; Xiang, J.; Liu, Z.; et al. Nonvolatile ferroelectric memory effect in ultrathin α-In_2Se_3. *Adv. Funct. Mater.* **2019**, *29*, 1808606.
(34) Wu, J.; Chen, H.-Y.; Yang, N.; Cao, J.; Yan, X.; Liu, F.; Sun, Q.; Ling, X.; Guo, J.; Wang, H. High tunnelling electroresistance in a ferroelectric van der Waals heterojunction via giant barrier height modulation. *Nat. Electron.* **2020**, *3*, 466−472.
(35) Han, W.; Zheng, X.; Yang, K.; Tsang, C. S.; Zheng, F.; Wong, L. W.; Lai, K. H.; Yang, T.; Wei, Q.; Li, M.; et al. Phase-controllable large-area two-dimensional In_2Se_3 and ferroelectric heterophase junction. *Nat. Nanotechnol.* **2023**, *18*, 55−63.
(36) Mak, K. F.; Ju, L.; Wang, F.; Heinz, T. F. Optical spectroscopy of graphene: From the far infrared to the ultraviolet. *Solid State Commun.* **2012**, *152*, 1341−1349.
(37) Youngblood, N.; Anugrah, Y.; Ma, R.; Koester, S. J.; Li, M. Multifunctional Graphene Optical Modulator and Photodetector Integrated on Silicon Waveguides. *Nano Lett.* **2014**, *14*, 2741−2746.
(38) Liu, L.; Dong, J.; Huang, J.; Nie, A.; Zhai, K.; Xiang, J.; Wang, B.; Wen, F.; Mu, C.; Zhao, Z.; et al. Atomically resolving polymorphs and crystal structures of In_2Se_3. *Chem. Mater.* **2019**, *31*, 10143−10149.
(39) Tao, X.; Gu, Y. Crystalline-crystalline phase transformation in two-dimensional In_2Se_3 thin layers. *Nano Lett.* **2013**, *13*, 3501−3505.
(40) Ding, W.; Zhu, J.; Wang, Z.; Gao, Y.; Xiao, D.; Gu, Y.; Zhang, Z.; Zhu, W. Prediction of intrinsic two-dimensional ferroelectrics in In_2Se_3 and other III_2-VI_3 van der Waals materials. *Nat. Commun.* **2017**, *8*, 14956.
(41) KüPers, M.; Konze, P. M.; Meledin, A.; Mayer, J.; Englert, U.; Wuttig, M.; Dronskowski, R. Controlled Crystal Growth of Indium Selenide, In_2Se_3, and the Crystal Structures of α-In_2Se_3. *Inorg. Chem.* **2018**, *57*, 11775−11781.
(42) Si, M.; Zhang, Z.; Chang, S.-C.; Haratipour, N.; Zheng, D.; Li, J.; Avci, U. E.; Ye, P. D. Asymmetric Metal/α-In_2Se_3/Si Crossbar Ferroelectric Semiconductor Junction. *ACS Nano* **2021**, *15*, 5689−5695.
(43) Wu, J. H.; Jian, J. L.; Sun, B. S.; Ye, Y. T.; Ma, H.; Tang, B.; Deng, Q. Y.; Tang, R. J.; Li, J. Y.; Sun, C. L.; Lin, H. T.; Li, L. Dual-function optical modulation and detection in microring resonators integrated graphene/$MoTe_2$ heterojunction. *Appl. Phys. Rev.* **2024**, *11*, 021426.
(44) Das, A.; Pisana, S.; Chakraborty, B.; Piscanec, S.; Saha, S. K.; Waghmare, U. V.; Novoselov, K. S.; Krishnamurthy, H. R.; Geim, A. K.; Ferrari, A. C.; Sood, A. K. Monitoring dopants by Raman scattering in an electrochemically top-gated graphene transistor. *Nat. Nanotechnol.* **2008**, *3*, 210−215.
(45) Majumdar, A.; Kim, J.; Vuckovic, J.; Wang, F. Electrical Control of Silicon Photonic Crystal Cavity by Graphene. *Nano Lett.* **2013**, *13*, 515−518.
(46) Geler-Kremer, J.; Eltes, F.; Stark, P.; Stark, D.; Caimi, D.; Siegwart, H.; Jan Offrein, B.; Fompeyrine, J.; Abel, S. A ferroelectric multilevel non-volatile photonic phase shifter. *Nat. Photonics* **2022**, *16*, 491−497.
(47) Taki, K.; Sekine, N.; Watanabe, K.; Miyatake, Y.; Akazawa, T.; Sakumoto, H.; Toprasertpong, K.; Takagi, S.; Takenaka, M. Nonvolatile optical phase shift in ferroelectric hafnium zirconium oxide. *Nat. Commun.* **2024**, *15*, 3549.
(48) Alexander, K.; George, J. P.; Verbist, J.; Neyts, K.; Kuyken, B.; Van Thourhout, D.; Beeckman, J. Nanophotonic Pockels modulators on a silicon nitride platform. *Nat. Commun.* **2018**, *9*, 3444.
(49) Sorianello, V.; Midrio, M.; Contestabile, G.; Asselberghs, I.; Van Campenhout, J.; Huyghebaert, C.; Goykhman, I.; Ott, A.; Ferrari, A.; Romagnoli, M. Graphene-silicon phase modulators with gigahertz bandwidth. *Nat. Photonics* **2018**, *12*, 40−44.

https://doi.org/10.1021/acs.nanolett.4c02625
Nano Lett. 2024, 24, 11469−11475